



# The Sea State CCI dataset v1 : towards a Sea State Climate Data Record based on satellite observations

Guillaume Dodet<sup>1</sup>, Jean-François Piolle<sup>1</sup>, Yves Quilfen<sup>1</sup>, Saleh Abdalla<sup>2</sup>, Mickaël Accensi<sup>1</sup>, Fabrice Ardhuin<sup>1</sup>, Ellis Ash<sup>3</sup>, Jean-Raymond Bidlot<sup>2</sup>, Christine Gommenginger<sup>4</sup>, Gwendal Marechal<sup>1</sup>, Marcello Passaro<sup>5</sup>, Graham Quartly<sup>6</sup>, Justin Stopa<sup>7</sup>, Ben Timmermans<sup>4</sup>, Ian Young<sup>8</sup>, Paolo Cipollini<sup>9</sup>, and Craig Donlon<sup>10</sup>

<sup>1</sup>Laboratoire d'Océanographie Physique et Spatiale (LOPS), CNRS, IRD, Ifremer, IUEM, Univ. Brest, France

<sup>2</sup>European Centre for Medium-range Weather Forecasts, Reading, United Kingdom

<sup>3</sup>Satellite Oceanographic Consultants (SatOC), Coach House Farm, New Mills, Derbyshire, UK

<sup>4</sup>National Oceanography Centre (NOC), European Way, Southampton SO14 3ZH, United Kingdom

<sup>5</sup>Deutsches Geodätisches Forschungsinstitut der Technischen Universität München (DGFI-TUM), Arcisstrasse 21, 80333, München, Germany

<sup>6</sup>Plymouth Marine Laboratory (PML), Prospect Place, The Hoe, Plymouth, Devon, PL1 3DH, UK

<sup>7</sup>Department of Ocean Resources and Engineering, School of Ocean and Earth Science and Technology, University of Hawaii at Manoa, Honolulu, HI, USA

<sup>8</sup>Department of Infrastructure Engineering, University of Melbourne, Melbourne, Australia

<sup>9</sup>Telespazio VEGA UK for ESA Climate Office, ECSAT, Fermi Avenue, Harwell Campus Didcot, OX11 0FD, United Kingdom

<sup>10</sup>ESA Climate Office, ECSAT, Fermi Avenue, Harwell Campus Didcot, OX11 0FD, United Kingdom

**Correspondence:** Guillaume Dodet (guillaume.dodet@ifremer.fr)

**Abstract.** Sea state data are of major importance for climate studies, marine engineering, safety at sea, and coastal management. However, long-term sea state datasets are sparse and not always consistent, and sea state data users still mostly rely on numerical wave models for research and engineering applications. Facing the urgent need for a sea state Climate Data Record, the Global Climate Observing System has listed "Sea State" as an Essential Climate Variable (ECV), fostering the launch in 2018 of the Sea State Climate Change Initiative (CCI). The CCI is a program of the European Space Agency, whose objective is to realize the full potential of global Earth Observation archives established by ESA and its member states in order to contribute to the ECV database. This paper presents the implementation of the first release of the Sea State CCI dataset, the implementation and benefits of a high-level denoising method, its validation against in-situ measurements and numerical model outputs, and the future developments considered within the Sea State CCI project. The Sea State CCI dataset v1 is freely available on the ESA CCI website (<http://cci.esa.int/data>) at [ftp://anon-ftp.ceda.ac.uk/neodc/esacci/sea\\_state/data/v1.1\\_release/](ftp://anon-ftp.ceda.ac.uk/neodc/esacci/sea_state/data/v1.1_release/). Three products are available: a multi-mission along-track L2P product (<http://dx.doi.org/10.5285/f91cd3ee7b6243d5b7d41b9beaf397e1>, Piollé et al., 2020a), a daily merged multi mission along-track L3 product (<http://dx.doi.org/10.5285/3ef6a5a66e9947d39b356251909dc12b>, Piollé et al., 2020b) and a multi-mission monthly gridded L4 product (<http://dx.doi.org/10.5285/47140d618dcc40309e1edbc7e773478>, Piollé et al., 2020c).



## 1 Introduction

Sea state is a key component of the coupling between the ocean and the atmosphere, the coasts and the sea ice. In the open ocean, wind-generated waves increase the sea surface roughness and enhance the air-sea momentum transfer through the modification of the wind stress (Edson et al., 2013). Wave breaking contribute to the mixing of the ocean upper layer (Babanin and Haus, 2009) and release of sea spray aerosol into the atmosphere (Monahan et al., 1986). At the coast, waves are refracted by the shallow bathymetry and the tidal currents, they shoal over the shoreface and transfer energy to higher and lower harmonics through nonlinear interactions (Longuet-Higgins and Stewart, 1962). They eventually break in the surf zone, increasing the water level, generating strong currents and stirring large quantities of sediments at the break point (Thornton et al., 1996). All these wave-induced processes contribute to rapid coastal erosion (Masselink et al., 2016), dune breaching (Kraus and Wamsley, 2003) and/or low-lying land overwash during extreme storm events. In the high latitudes, waves interact with the sea ice by modifying its mechanical properties, through the fragmentation of the ice floes of the marginal ice zone into smaller pieces, or through the push of the ice in the direction of the wave propagation (Stopa et al., 2018). Given that increased greenhouse gas emission caused by anthropic activities has a strong impact on the Earth's climate, which translates into the modification of the atmospheric circulation, the acceleration of sea level rise and the rapid decay of Arctic sea ice, significant changes in future sea state conditions and the above-mentioned coupling mechanisms are expected.

Nowadays, long-term records of wave parameters are provided by Voluntary Observing Ships along the major maritime routes (Gulev and Grigorieva, 2004), by in-situ wave buoy networks, mostly located along the US, European, Japanese and Australian coastlines, and by satellite altimeter measurements (Ribal and Young, 2019). While altimeter-based datasets are providing the (almost) global coverage necessary to understand the large-scale variability of sea states and their interactions with the other components of the Earth's climate, they still suffer from several limitations: 1) the principal sea state parameter deduced from radar altimeter echoes is the significant wave height, yet other spectral parameters such as the wave period and directions are key for some applications, e.g. coastal impacts; 2) altimeter measurements cover the last 34 years only (starting with GEOSAT in 1985 with a data gap between 1990 and 1991), which is still relatively short to extract robust trend information out of the strong multi-annual fluctuations of the significant wave height; 3) altimeter missions need to be accurately cross-calibrated to deliver consistent long-term time-series, this is particularly true when instruments operating in different modes are merged in a single product; 4) altimeter measurements are contaminated by different sources of noise, which prevent a proper representation of SWH variability at scale lower than 100 km (Ardhuin et al., 2017). In the last 20 years, several research groups have contributed to the development of long-term calibrated altimeter databases (Queffelec, 2004; Zieger et al., 2009; Ribal and Young, 2019), and some of these datasets have been used to compute the significant wave height trends over the last decades. In a recent study, Young and Ribal (2019) estimated trends in SWH ranging from  $-1$  to  $+1$   $\text{cm}\cdot\text{year}^{-1}$ , depicting a large regional variability with negative trends mostly located in the Pacific Ocean. These results, and the dataset they are based on (Ribal and Young, 2019), represent a milestone in the characterization of sea state decadal variability, however, new developments are necessary to verify these findings and extend the potential of satellite sea state observations.



Aware of the increasing need for accurate, robust and consistent long term sea state data required by the climate science community (Ardhuin et al., 2019), the Global Climate Observing System (GCOS) has listed "Sea State" as an Essential Climate Variable (ECV). ECVs are geophysical records generated from systematic Earth Observations in support of the international frameworks and policies such as the work of the United Nations Framework Convention on Climate Change (UNFCCC) and the Intergovernmental Panel on Climate Change (IPCC). The Climate Change Initiative program, launched by the European Space Agency in 2010, has already contributed to the production of new Climate Data Records (CDR) associated with ECVs (e.g. aerosol, Popp et al. (2016), sea ice concentration, Lavergne et al. (2019)). In this context, the Sea State CCI+ project was kicked off in 2018 in order to produce a CDR for the new ECV "Sea State". This paper presents the first dataset released in the context of the Sea State CCI+.

The first section of this paper describes the altimeter missions that have been considered for the Sea State CCI dataset v1, and the in-situ and model data that have been used to compare against the altimeter data. Section 2 describes the main processing steps (namely, data editing, inter-calibration and denoising) implemented within the Sea State CCI production system. Section 3 presents the results of the comparison against model and in-situ data, and Section 4 addresses the quality control applied to the data. Section 5 presents a short introduction to two potential applications of Sea State CCI dataset v1 at global and regional scales. Finally, Section 6 discusses the current status of the CCI dataset v1, the main limitations of the data and the perspectives for the future releases of this dataset.

## 2 Data and Methods

### 2.1 Altimeter data

The altimeter data used in the Sea State CCI dataset v1 come from multiple missions spanning from 1991 to 2018. Many altimeters are bi-frequency for atmospheric corrections (Ku-C or Ku-S) and only measurements in Ku band were used, for consistency reasons, being available on each altimeter except SARAL/AltiKa (Ka band). Table 1 provides the list of missions used in the Sea State CCI dataset v1, together with the input product and version used, and their orbital properties (note that some cycle changes occurred in the course of some missions for limited period of times : these are not listed here for clarity but the corresponding measurements were included in the Sea State CCI dataset v1). Not surprisingly, the list of altimeter data sources is very similar to that used by the Sea Level CCI (see Fig. 1a of Quartly et al. (2017), except that project could not utilise the instruments in very long repeat cycles.

### 2.2 In-situ measurements

The in-situ data used to validate the Sea State CCI dataset v1 were gathered by ECMWF (Figure 1). Most of the data came from the operational archive from ECMWF, where all data distributed via the Global Telecommunication System (GTS) are kept. Data from moored buoys and fixed platforms were extracted. These data are usually reported hourly (or less frequently). The bulk of the data comes from moored buoys, with the exception of data from operating platforms in the North and Norwegian



**Table 1.** List of altimeter missions used for the Sea State CCI dataset v1

Mission	Instrument	Band	Covered period	Repeat period (days)	Altitude (km)	Inclination (°)	Source product
ERS-1	RA	Ku	1991-2000	35	785	98.52	OPR [ESA/F-PAF]
TOPEX	NRA	Ku	1992-2006	10	1336	66	MGDR [CNES]
ERS-2	RA	Ku	1995-2011	35	785	98.52	OPR [ESA/F-PAF]
GFO	GFO-RA	Ku	1998-2008	17	800	108	GDR/POE [NOAA]
JASON-1	Poseidon-2	Ku	2001-2013	10	1336	66	GDR vE [AVISO]
ENVISAT	RA-2	Ku	2002-2012	35	799	98.55	GDR v2.1 [ESA/F-PAC]
JASON-2	Poseidon-3	Ku	2008-2019	10	1336	66	GDR vD [AVISO]
CRYOSAT-2	SIRAL	Ku	2010-Ongoing	369	717	92	IGDR [NOAA]
SARAL	AltiKa	Ka	2013-Ongoing	35	785	98.55	GDR [AVISO]
JASON-3	Poseidon-3B	Ku	2016-Ongoing	10	1336	66	GDR vD [AVISO]

Seas and the Gulf of Mexico. The main data providers are the US, via the National Data Buoy Center (NDBC) and Scripps, Canada, the UK, France, Ireland, Norway, Iceland, Germany, Spain, Brazil, South Korea, and India. This dataset was supplemented by buoy data obtained from the web sites from the UK Centre for Environment, Fisheries and Aquaculture Science (CEFAS) and the Faeroe Islands network. In addition, buoy data from Denmark, New-Zealand and Japan obtained as part of ECMWF wave forecast validation project were also used. A basic quality control was applied to each hourly time series for each location to remove spurious outliers.

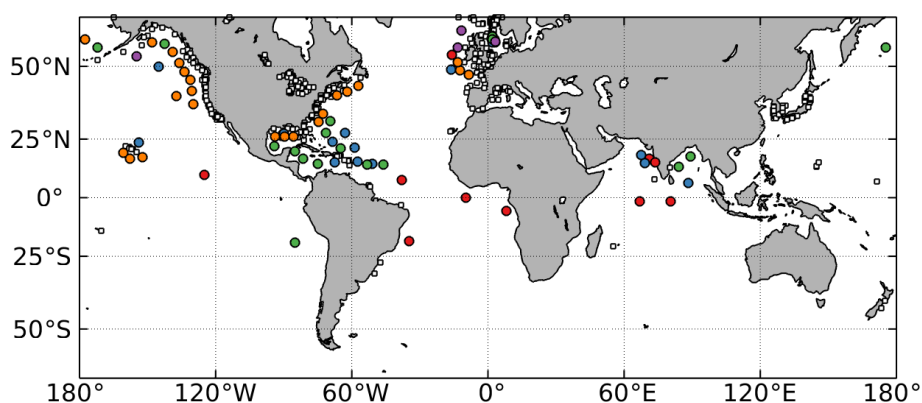


**Figure 1.** Global maps of the wave in-situ locations used for the Sea State CCI project. White squares represent all wave in-situ locations gathered by ECMWF. Colored circles indicate buoys located > 200km offshore, used to validate the Sea State CCI dataset v1. Colors indicate the time period covered by each buoy: 0-5 years (red), 5-10 years (blue), 10-15 years (green), 15-20 years (purple), 20-25 years (orange)



Wave in-situ measurements were compared to altimeter data at every altimeter-insitu match-up. An altimeter-insitu match-up occurs each time the altimeter ground track is less than 50 km from a in-situ location and the in-situ measurement is available within 30-min (following Queffelec, 2004). For each match-up, the altimeter SWH is averaged over the along-track records lying within a 50-km-radius-circle centered on the in-situ location and the in-situ time-series is filtered with a 1-hr moving window. The nearest (in time) record is then stored for comparisons with the averaged altimeter SWH. The metrics used for validations are the bias, the root mean square error (RMSE), the RMSE normalized by the mean of the buoy observations (NRMSE), the scatter index (SI) and the correlation coefficient (R). Comparisons between altimeter data and in-situ measurements showed much better agreement when coastal buoys (<200 km) were discarded from the analysis. This can be seen, for instance, on the scatter diagram and error metrics computed between SARAL and in-situ SWH measurements during the year 2017 (Figure 2), when all wave buoys are considered (left panel), and when only offshore wave buoys 200 km away from the coast are considered (right panel). Poorer performances in the comparison with coastal buoys have at least three reasons: firstly, land shading and refraction can modify SWH at much shorter distances than in the open ocean, affecting the validity of the 50-km-radius assumption and jeopardising the number of sites that can be effectively used for the comparison; secondly, coastal backscatter inhomogeneities in the satellite footprint affects the retrievals particularly in the last 20 km from the coastline (see section 6.2); finally, the stronger variability of the wave field in the coastal zone due to tidal currents, bathymetric refraction, coastal wind in-homogeneity invalidates the assumption of wave field homogeneity within the altimeter footprint. Therefore, the validation of altimeter SWH was performed on a reduced data set including only offshore buoys located more than 200 km from the coast.

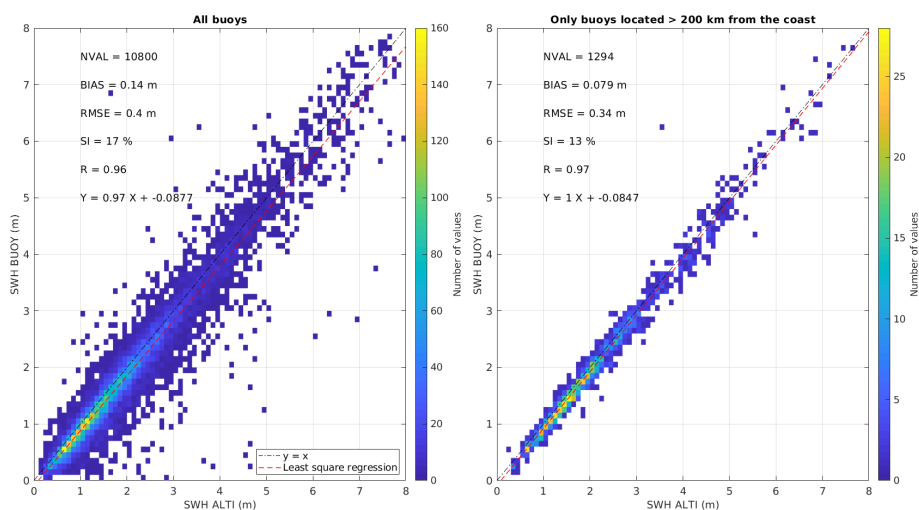


**Figure 2.** Comparison between SARAL and wave in-situ SWH measurements during year 2017, when all in-situ sites are considered (left) and when only locations 200 km away from the coast are considered (right).



### 2.3 Numerical wave model

The wave hindcasts used to compare model results with altimeter data were produced with the spectral wave model WAVEWATCH III © (WW3, The WAVEWATCH III Development Group, 2016). The model is forced by wind fields from the ERA5 (Hersbach et al., 2018), by geostrophic and Ekman current components from Globcurrent products (Rio et al., 2014), with an ice mask applied from SSMI radiometer (Wentz et al., 2012) and iceberg distribution from Altiberg (Tournadre et al., 2016). The coverage is global and extends from 78°S to 80°N at 0.5° resolution with a spectral discretization of 24 directions and 36 frequencies with lowest frequency at 0.0339Hz. Output fields are generated at 3-hourly intervals. The WW3 version used is based on github NOAA-EMC stable released from June 27, 2019. The model parameterization is based on Rasclé and Ardhuin (2013) (T471) with following tuning for the wave growth : BETAMAX=1.65, SWELLF7 =  $4.14 \times 10^5$  and for the strong wind intensification : WCOR1=23., WCOR2=1.08. Modelled SWH values are linearly interpolated along the satellite ground track and statistical errors (bias, RMSE, NRMSE, SI, R) are then computed. Statistics are only computed on measurements considered as good, based on the quality level flag defined in Section 3.1 and a threshold distance of 50 km from the coastline.

### 3 Processing of altimeter data

The Sea State CCI dataset v1 products are inherited from the GlobWave project (2009-2012) building on the experience and methodology developed within this project. It extends and improves the GlobWave products which were a post-processing of existing L2 altimeter agency products with additional filtering, corrections and variables. Three kinds of products are delivered in the Sea State CCI dataset v1:

- L2P : Along-track products separated per satellite and half-orbit (pass) or full orbit (depending on the input product used), including all measurements with flags, corrections and extra parameters from other sources. These are expert products with rich content and no data loss (Piollé et al., 2020a);
- L3 : Edited merged daily products, derived from the L2P and retaining only valid and good quality measurements from all altimeters over one day (one daily file), with simplified content (only a few key parameters). This is close to what is delivered in near real time by, for instance, the Copernicus Marine Environment Monitoring Service (Piollé et al., 2020b);
- L4 : Statistical gridded products, also derived from the L2P and averaging valid and good measurements from all available altimeters over a fixed resolution grid ( $1^\circ \times 1^\circ$ ) on a monthly basis. These products are meant for statistics and visualization (such as the CCI toolbox, <http://climatetoolbox.io/>) (Piollé et al., 2020c).

The following sections provide more details on the processing steps of L2P products, from which L3 and L4 are derived.



### 3.1 Data editing

This first step consists in the identification of bad or suspect measurements, in order to build a quality level flag (*quality\_level*) providing users with a way to only retain the valid measurements in their analysis. This is achieved through a series of tests applied to each measurement, the result of which are summarized into an additional rejection flag (*swh\_rejection\_flags*), where each bit documents a specific test's failure or success. Table 2 lists the four levels of the variable *quality\_level*.

**Table 2.** Quality levels defined for Sea State CCI dataset v1

Value	Meaning	Description
0	undefined	the measurement value is not defined or relevant (missing value, etc. . . ), no quality check was applied.
1	bad	the measurement was qualified as not usable after quality check.
2	acceptable	the measurement may be usable for specific applications only or the quality check could not fully assess if it is a bad or good value (suspect).
3	good	the measurement is usable.

When SWH measurements were rejected as bad, the reason (quality test) for which they were rejected is reported in the related *swh\_rejection\_flags* variable. The eight rejection flags are the following:

- **not\_water**: The surface type is not water. It may be land, continental ice,.... We try to keep lake and inner seas measurements (when the discrimination is possible from the GDR information). This test only uses the internal flags provided in the input product by the producer.
- **sea\_ice**: The measurement has possible ice contamination. The sea ice fraction is taken from an external source (such as the CCI Sea Ice microwave based daily maps). Sea ice contamination is defined as areas where the sea ice fraction is greater than a minimal threshold (corresponding to 10% of ice in the current configuration). SWH measurements where the sea ice fraction is greater than 0% but lower than 10% are classified as *acceptable*.
- **swh\_validity**: The SWH measurements were considered as invalid (for instance because of the possible range or some internal flag provided in the original product used as input).
- **sigma0\_validity**: The sigma0 measurements were considered as invalid for water surface type.
- **waveform\_validity**: The measurements were considered as invalid as there are indications of unsuitable waveforms (as indicated in some internal flag provided in the original product used as input) for a proper SWH calculation.
- **ssh\_validity**: The SWH measurements were considered as invalid as there were issues on SSH (as indicated in some internal flag provided in the original product used as input) which was considered as an indication of problematic quality for SWH too.





- **swh\_rms\_outlier**: The root mean square deviation of the 20 Hz SWH measurements exceeds a certain threshold, which depends on SWH and is computed following Sepulveda et al. (2015)
- **swh\_outlier**: The measurements were considered as invalid when performing the SWH outlier test: this test considers all the measurements within a 100km window centered on the screened measurement; measurements that deviate from the 100-km mean (excluding the two most extreme values in the mean calculation) by more than 3.9 standard deviation or by more than 5 meters are discarded. This step is iterated three times over the same window.

The editing criteria which leads to setting the SWH quality level and rejection flags are specific to each mission and are detailed in the Sea State CCI dataset product user guide.

### 3.2 Cross-calibration

10 The Sea State CCI project builds on the GlobWave project, for which SWH altimeter measurements over the period 1985-2016 were carefully calibrated against in-situ data (GlobWaveTeam, 2013). In the Sea State CCI dataset v1, three additional altimeter missions, namely JASON-3, CRYOSAT-2 and SARAL, have been included and we describe here the methodology used to cross-calibrate these SWH records against a common reference dataset. Moreover, a new version (version E) of the JASON-1 GDR has been released since the GlobWave project and the calibration formula derived for JASON-1 has also been updated.

15 According to the GlobWave Annual Quality Control Report (GlobWaveTeam, 2012), there is no specific quality problem in JASON-2 and the variability in terms of data quality is lower than for JASON-1 and ENVISAT. Therefore, the calibrations of JASON-1, JASON-3, CRYOSAT-2 and SARAL are performed against the JASON-2 data, as calibrated by Queffeuilou and Croizé-Fillon (2017). Altimeter SWH cross-calibration is carried out by comparing SWH measurements at cross-over locations between the altimeter to be calibrated and the reference mission JASON-2. A cross-over data pair is defined each time the two

20 satellite ground tracks intersect within a 60-min time window (Fig. 3). In order to attenuate the impact of along-track noise (instrumental and retracking-induced noise) in the comparison, SWH is averaged along  $n$  consecutive measurements 25-km apart of the intersection points ( $7 \leq n \leq 9$  depending on altimeter orbital velocity, shown as blue and red dots on Figure 3). SWH at cross-over locations are then compared to estimate the calibration formula. Visual assessment of JASON-1, JASON-3 and SARAL SWH measurements against JASON-2 calibrated SWH measurements indicate a linear relationship between

25 these missions (Figures 4, 5 and 6) and linear calibration formula are obtained by fitting a least-square regression line through the SWH data. Note that the fitting was only applied for SWH values larger than 1 m. Below this value, the linearity of the relationship is lost, mostly due to differences in the instrumental correction applied to account for the fact that the point target response in the model used to is approximated by a Gaussian function (Thibaut et al., 2010). Moreover, it is known that SWH retrieval at low sea states and particularly below 0.75 m is less accurate and noisier due the inadequate sampling of

30 the signal (Smith and Scharroo, 2015). For CRYOSAT-2 the relationship is no longer linear (Figure 7) and we use a second-order polynomial function to correct this mission. In order to avoid discontinuous and unrealistic corrections at high sea state, we apply this second-order polynomial corrections until an upper threshold, corresponding to the SWH values at which the



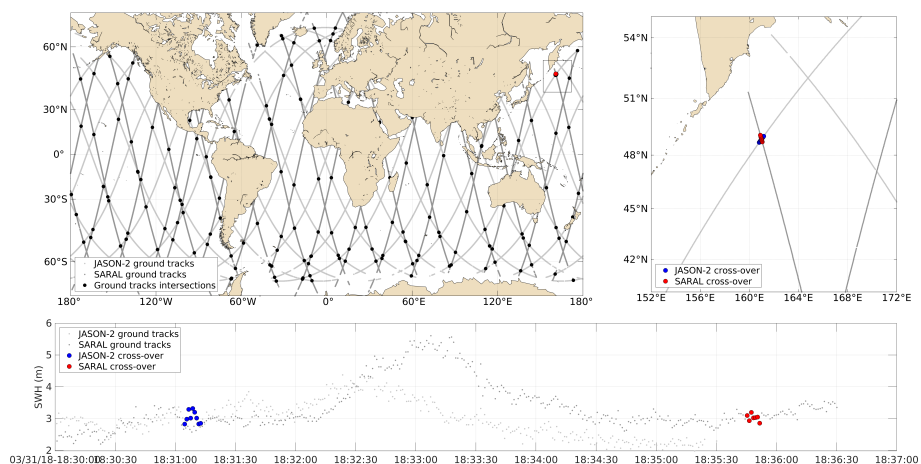


**Figure 3.** [Top-left panel] JASON-2 (light grey) and SARAL (dark grey) ground tracks on March 31 2018 with ground track intersection shown with black circles. [Top right panel] Zoom on a ground track cross-over occurring within 60 min. Bottom panel. Time-series of the crossing-over along-track SWH shown in the top right panel.

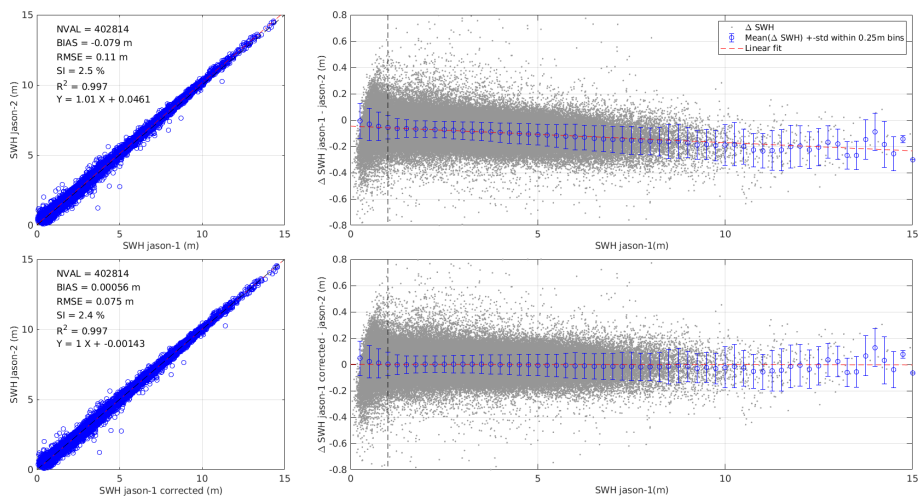


**Figure 4.** (Left) Scatter diagrams of JASON-2 SWH against JASON-1 SWH before (top) and after (bottom) calibration. (Right) Residual of JASON-1 SWH – JASON-2 SWH as a function of JASON-1 SWH before (top) and after (bottom) calibration. The red dashed line is a linear fit through the data.

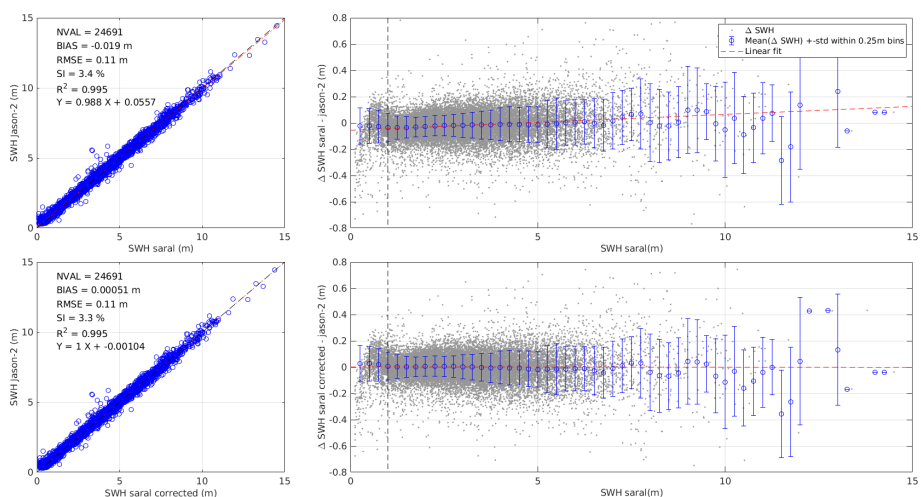


**Figure 5.** (Left) Scatter diagrams of JASON-2 SWH against SARAL SWH before (top) and after (bottom) calibration. (Right) Residual of SARAL SWH – JASON-2 SWH as a function of SARAL SWH before (top) and after (bottom) calibration. The red dashed line is a linear fit through the data.

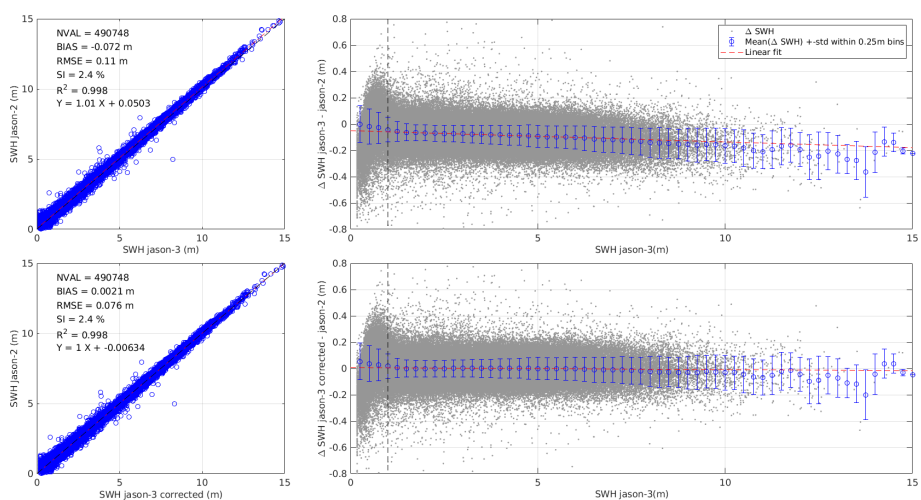


**Figure 6.** (Left) Scatter diagrams of JASON-2 SWH against JASON-3 SWH before (top) and after (bottom) calibration. (Right) Residual of JASON-3 SWH – JASON-2 SWH as a function of JASON-3 SWH before (top) and after (bottom) calibration. The red dashed line is a linear fit through the data.

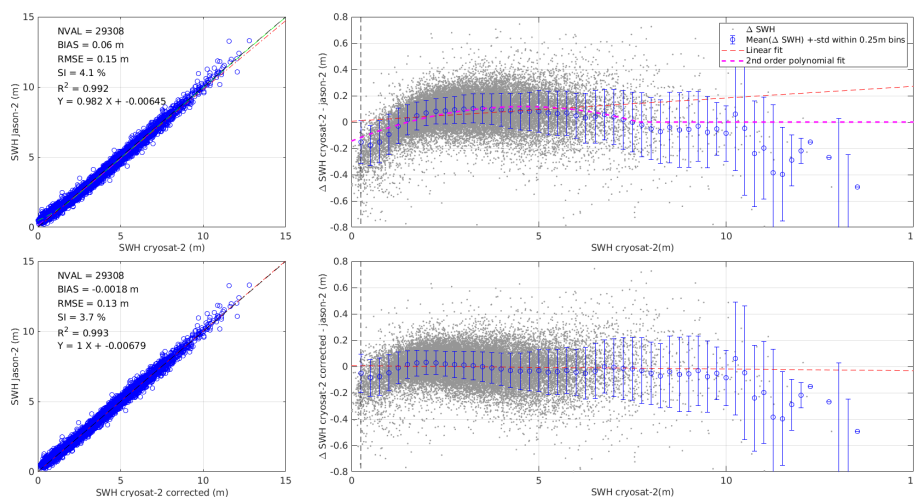


**Figure 7.** (Left) Scatter diagrams of JASON-2 SWH against CRYOSAT-2 SWH before (top) and after (bottom) calibration. (Right) Residual of CRYOSAT-2 SWH – JASON-2 SWH as a function of CRYOSAT-2 SWH before (top) and after (bottom) calibration. The red dashed line is a linear fit through the data.

polynomial intersects the zero residual y-axis (in this case 7.67 m). Table 3 lists the equations used to calibrate the altimeter SWH measurements in the Sea State CCI dataset v1.

**Table 3.** Calibration formula used for the Sea State CCI dataset v1

Mission	Calibration formula	Applied to
ERS-1	$SWH_{cal} = 1.1259SWH + 0.1854$	All data
TOPEX	$SWH_{cal} = 1.0539SWH - 0.0766$	cycles 0-97
	$SWH_{cal} = 1.0539SWH - 0.0766 + dh(cycle)^{(1)}$	cycles 98-235
	$SWH_{cal} = 1.0237SWH - 0.0476$	cycles > 235
ERS-2	$SWH_{cal} = 1.0541SWH + 0.0391$	All data
GFO	$SWH_{cal} = 1.0625SWH + 0.0754$	All data
JASON-1	$SWH_{cal} = 1.0125SWH + 0.0461$	All data
ENVISAT	$SWH_{cal} = -0.021SWH^3 + 0.1650SWH^2 + 0.5693SWH + 0.4358$	$SWH < 3.41 m$
	$SWH_{cal} = 1.0095SWH + 0.0391$	$SWH \geq 3.41 m$
JASON-2	$SWH_{cal} = 1.0149SWH + 0.0277$	All data
CRYOSAT-2	$SWH_{cal} = 0.0124SWH^2 + 0.8858SWH + 0.1446$	$SWH < 7.67 m$
SARAL	$SWH_{cal} = 0.9881SWH + 0.0555$	All data
JASON-3	$SWH_{cal} = 1.0086SWH + 0.0503$	All data

<sup>(1)</sup>  $dh = -0.0685 + 6.0426 \cdot 10^{-4} cycle + 7.7894 \cdot 10^{-6} cycle^2 - 6.9624 \cdot 10^{-8} cycle^3$



### 3.3 Data denoising

Altimeter measurements are characterized by a low signal-to-noise ratio (SNR) at spatial scales below about 100 km, blurring geophysical signals in this scale range, such as those resulting from wave-current interactions. The use of altimeter data therefore often requires preliminary noise filtering, and low-pass or smoothing filters are frequently applied. Such operation quite systematically results in the loss of small-scale (< 100 km) geophysical information, in the creation of artifacts in the geophysical variability analyzed (e.g. spectral ringing), and requires setting of a cut-off wavelength or filter window length that is difficult to determine adequately for a global data set. As for approaches that infer a correction to eliminate correlated errors from other aspects of the waveform data (Quartly, 2019; Tran et al., 2019), it also leaves a substantial amount of low- and medium-frequency noise in the data. To overcome these difficulties, an adaptive noise elimination method is used, based on the non-parametric Empirical Mode Decomposition (EMD) method developed to analyze non-stationary and non-linear signals (Huang et al., 1998). EMD is a scale decomposition into a limited number of amplitude and frequency modulated functions (AM/FM) - called Intrinsic Mode Functions (IMF) - among which the Gaussian noise distribution is predictable (Flandrin et al., 2004). It therefore provides the basis for a noise elimination approach with results often superior to those of wavelet-based techniques (Kopsinis and McLaughlin, 2009). Recently, EMD analysis has been successfully applied to altimeter data to analyze wave-current interactions known to predominate at scales below 100 km (Quilfen et al., 2018; Quilfen and Chapron, 2019). For reference the method is fully described in (Quilfen and Chapron, 2020).

#### 3.3.1 The EMD principles

EMD adaptively decomposes a signal  $x(t)$  into a small number  $L$  of IMFs  $h_n(t)$ ,  $1 \leq n \leq L$ , so that:

$$x(t) = \sum_{n=1}^L h_n(t) \quad (1)$$

The IMF number,  $L$ , depends on the length of the record and typically varies from 1 to 10 for the lengths analyzed in the altimeter dataset. By construction, IMFs have the following properties: they are zero mean, all their maxima and minima are respectively positive and negative, and they have the same number (or  $+/-1$ ) of zero-crossings and local extrema. The IMFs are calculated successively, the first containing the shortest scales by the construction of the algorithm. Each IMF is estimated using an iterative process called sifting that determines the AM/FM high-frequency part of any input signal. For a given data segment, the sifting operates in a few steps: 1) find the local maxima and minima; 2) interpolate along the maxima and minima to form an upper and a lower envelope; 3) calculate the average of the two envelopes and subtract it from the analyzed segment; 4) repeat the process from step 1 to 3 unless a stopping criterion has been met (see Huang et al., 1998; Quilfen and Chapron, 2020, for details). An example is shown in Figure 8 for a JASON-2 measurements record of about 1060-km length, for which the EMD method determined six IMFs to represent the full signal. The figure also shows other aspects of the denoising process to be discussed in the next section. As shown, the high-frequency noise is projected in the first IMF, and the scale range of each IMF is increasing with the IMF increasing rank. Notably, the very large geophysical gradients such as observed in this example are also captured by IMF1. IMF1 therefore requires a particular processing to separate noise from useful information.

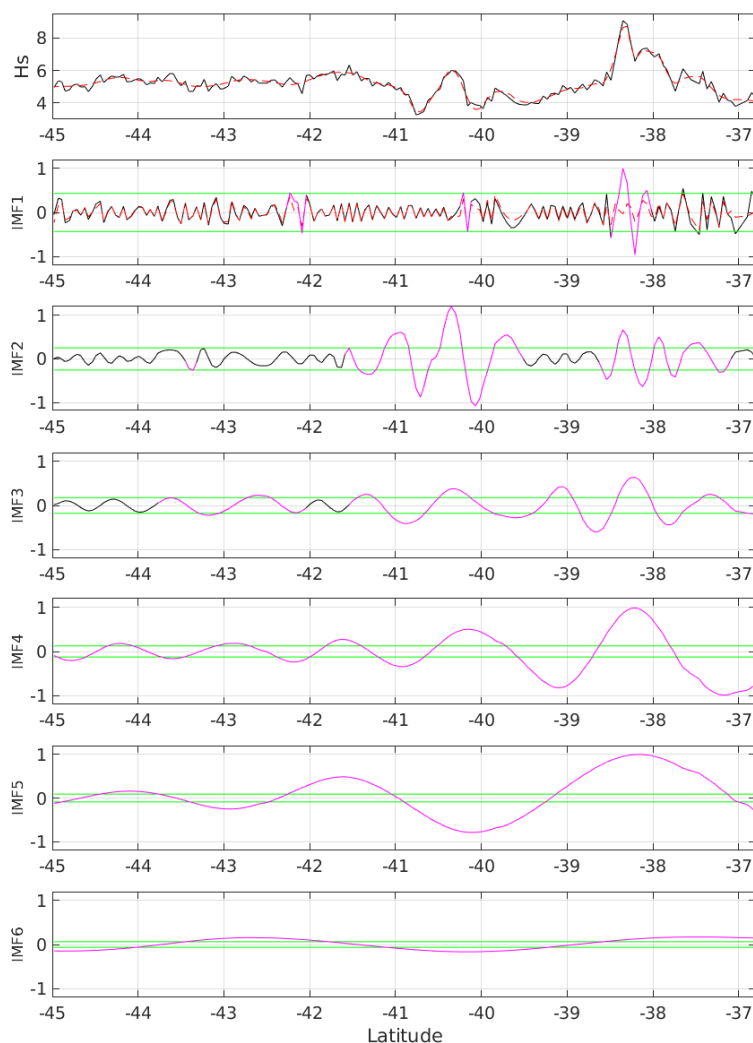


**Figure 8.** EMD expansion in  $L$  IMFs (panels 2 to 6 from top to bottom) for a data segment of JASON-2 raw (black solid line) and filtered (dashed red line) SWH measurements (upper panel, February 29, 2016). For the IMFs, the black lines show the IMF amplitudes and the superimposed magenta lines the signal portions identified as above the predicted noise level (green solid lines). For this particular case, portions of signal that are dominated by noise are found solely in the three first IMFs. For IMF1, the dashed red line shows the high-frequency noise series that has been computed from IMF1 wavelet processing. As obtained, six IMFs describe the total signal.



Once the signal is broken down into a set of IMFs, a denoising strategy inspired by those used for wavelet techniques can be applied. The analysis to be carried out takes advantage of 1) the well-behaved and predictable distribution of Gaussian noise energy with the IMF basis, 2) the legacy of decades of wavelet-based denoising techniques, and 3) an ensemble average approach to estimate a robust noise-free signal.

### 5 3.3.2 EMD-based data denoising

Flandrin et al. (2004) showed that in the case of pure fractional Gaussian noise, the first IMF possesses the characteristics of a high-pass filter while the higher order modes behave similarly to a dyadic filter bank for which as descending the frequency scale, the successive frequency bands have half the width of their predecessors. This is illustrated in Figure 9.

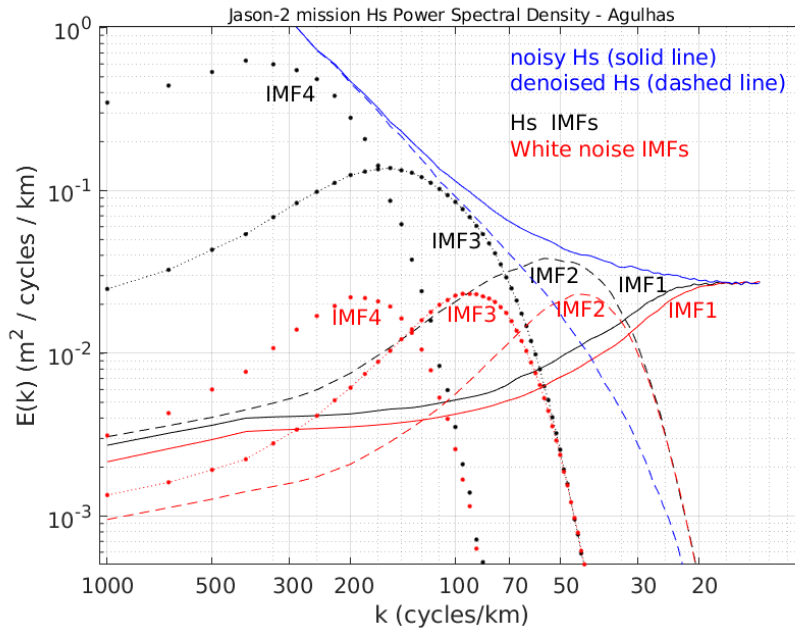


**Figure 9.** Mean Power Spectral Density (PSD) of the first four IMFs for white noise (red curves) and JASON-2 *SWH* along-track measurements (black curves), and mean PSD of the corresponding noisy (solid blue line) and denoised (dashed blue line) JASON-2 *SWH* measurements. The PSD is the average of PSDs computed over all data segments covering the years 2014 to 2016 in the Agulhas region (10°E – 35°E; 45°S – 33°S). From Quilfen and Chapron (2020).

It implies that the Gaussian noise variance projected onto the IMF basis can be modeled, for IMFs of rank  $n > 1$ , as follows:

10

$$\text{var}(h_n(t)) \propto 2^{(\alpha-1)n} \quad (2)$$

$\alpha$  depends on the autocorrelation function of the fractional Gaussian noise (i.e.,  $\alpha = 0.5$  for an uncorrelated noise, e.g., white noise;  $\alpha \neq 0.5$  for an autocorrelated noise). For a white noise, the expected noise energy level of each IMF of rank  $n > 1$  is then



given by:

$$E_n = \frac{E_1}{0.719} 2.01^{-n} \quad (3)$$

where  $E_1$  is computed using the Median Absolute Deviation (MAD) from zero:

$$E_1 = \left( \frac{\text{median}|n_1(t)|}{0.6745} \right)^2 \quad (4)$$

5 where  $n_1(t)$  is the IMF1 noise estimated from a wavelet analysis (as example see Figure 8, top panel). Eq. 3 and 4 then give the expected noise energy in each IMF to determine the different thresholds below which signal fluctuations are associated with noise, as illustrated in Figure 8. For each IMF, the threshold is  $T_n = A\sqrt{E_n}$ .  $A$  is a constant that can be adjusted as a global tuning parameter.

With the EMD basis, noise energy decreases rapidly with the increasing IMF rank: 59%, 20.5%, 10.3%, 5.2% of total  
10 energy for the first four IMFs, respectively, which represents 95% of the total noise energy. For a given noisy input signal, the SNR and robustness of the denoised signal (e.g. to mitigate for result uncertainties associated with signal fluctuations close to the applied thresholds) are increased by estimating the final result as an ensemble average of several denoised signals. For that, the noise  $n_1(t)$  is first removed from the noisy signal  $x(t)$ , then a set of  $k$  new noisy signals is generated by adding random realizations of  $n_1(t)$ , providing after denoising a set of  $k$  denoised signals whose average gives the resulting denoised SWH and  
15 whose standard deviation gives the uncertainty attached to the denoised SWH. The uncertainty parameter therefore accounts for the noise characteristics of the noisy signal (function of the altimeter sensor, SWH etc) as well as for the local SNR (which is scale-dependent) and for uncertainties attached to the denoising process.

Figure 9 illustrates the different points discussed above. It shows how the EMD filter bank distributes a white noise signal and the JASON-2 altimeter SWH signal in the Agulhas Current region. The standard deviation of noise was adjusted to fit  
20 the SWH background noise at scales  $< 20$  km. As shown, the EMD filter bank is composed of a high-pass filter, IMF1, and a dyadic filter bank for higher ranking IMFs. A similar structure is observed when EMD is applied to the SWH along-track signal, confirming that IMF1 contains mainly the high-frequency noise, and showing that pure noise and SWH higher ranking IMFs share the same frequency ranges. It highlights the practical rule for denoising that compares the signal modulation in each IMF with the noise energy expected for the same IMF rank. The proposed method is free of systematic artifacts, preserves  
25 the amplitude of spatial gradients and extreme values, and eliminates the noise over the whole frequency range. Signals down to scales of nearly 30 km can be recovered, provided that the local signal-to-noise ratio is sufficient.

## 4 Quality control

### 4.1 Validation against in-situ data and model results

Statistical metrics (bias, RMSE, NRMSE, SI and R) between altimeter measurements and in-situ data were computed for each  
30 mission, and each year, and the overall scores are provided in Table 4 for the denoised (and calibrated) SWH. With a number





of match-up data comprised between 1018 (ERS-1, 3 years of data) and 14395 (JASON-2, 11 years of data), all the computed values are statistically significant. Except for ERS-1 for which the bias is negative (-7.2 cm), all the mission show a positive bias lower than 10 cm. The RMSE is below 26 cm for all missions, corresponding to a mean value lower than 11% once normalized by the mean of the observations. Moreover the scatter index is lower than 9% and the correlation coefficient higher than 0.98 for all missions.

**Table 4.** Statistical metrics for the validation of denoised SWH in the Sea State CCI dataset v1 against in-situ data

Mission	N Years	Match-ups	Bias (m)	RMSE (m)	NRMSE (%)	SI (%)	R
ERS-1	3	1018	-0.072	0.259	9.946	8.409	0.984
TOPEX	12	7797	0.014	0.236	9.735	8.388	0.987
ERS-2	17	9207	0.014	0.239	10.408	8.957	0.985
GFO	9	5221	0.026	0.264	10.914	9.463	0.982
JASON-1	12	11094	0.010	0.221	9.584	8.310	0.986
ENVISAT	11	8286	0.044	0.234	10.052	8.582	0.985
JASON-2	11	14395	0.069	0.211	9.667	7.857	0.988
CRYOSAT-2	9	7913	0.069	0.197	9.168	7.462	0.989
SARAL	6	7876	0.088	0.214	10.141	7.956	0.988
JASON-3	3	4181	0.097	0.205	9.945	7.481	0.990

5

Comparison of the altimeter SWH against wave model hindcast was also performed as a complementary validation with an independent dataset. Figure 10 shows the globally-averaged bias and normalized RMSE between model and altimeter measurements for each mission of the Sea State CCI dataset v1. The bias between model and altimeter calibrated SWH is lower than 10 cm for all missions. The NRMSE for calibrated SWH is lower than 20% for ERS-1 and ERS-2 and lower than 15% for all other missions. In addition, we see that the denoised SWH parameter decreases the NRMSE between model results and hindcast respectively by up to 20% and by 10% on average.

Figure 11 presents the time-series of the mean global bias and mean global NRMSE for each altimeter mission over the period 1994-2018. In order to allow consistent comparisons between altimeters, only comparisons at latitudes lower than 60° were considered. We can see that the bias is comprised generally between 0-0.12 m, and increases significantly during the most recent years 2017 and 2018. The NRMSE is comprised between 11-14% over the period 1994-2007 for the missions ERS-1, ERS-2, ENVISAT, GFO and TOPEX, and between 10-12% over the period 2002-2018 for the remaining missions. These lower errors may be attributed to improvements in instruments and processing techniques.

## 4.2 Cross-consistency analysis

In order to ensure that the calibrated altimeter SWH are consistent over the whole time period covered by altimeter measurements, we computed the monthly global mean of calibrated SWH for each mission, within 60°S and 60°N. Figure 12

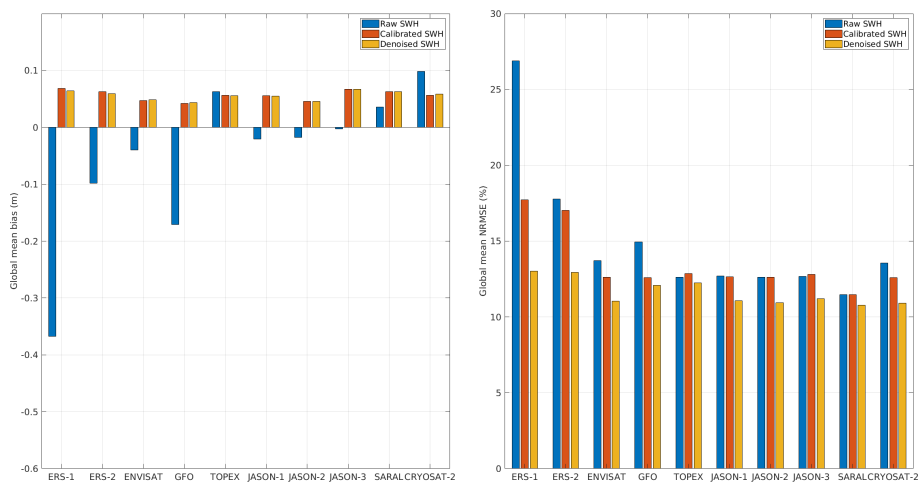


**Figure 10.** Global mean bias (left) and global mean NRMSE (right) between altimeter measurements and wave model hindcast.

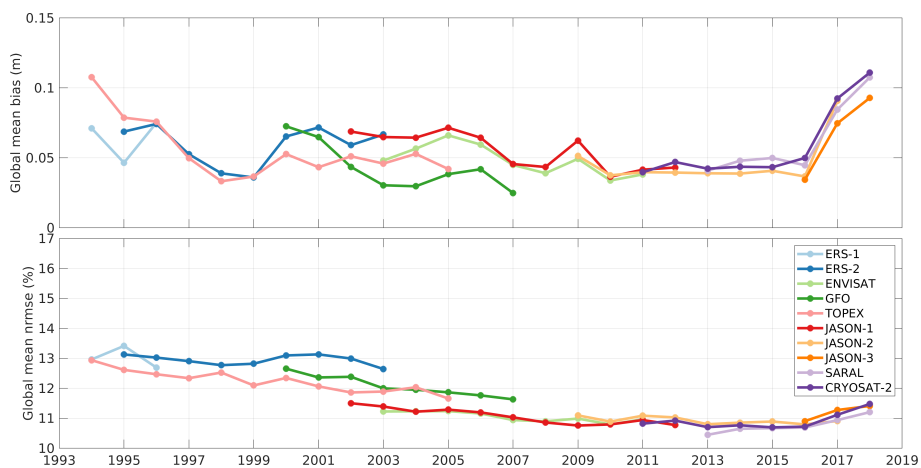


**Figure 11.** Time series of mean global bias (upper panel) and mean global NRMSE (lower panel) between Sea State CCI dataset v1 and WW3 model outputs forced with ERA5 wind fields.



shows time-series of global monthly means of un-calibrated and calibrated SWH over 1991–2018, revealing how calibration of altimeter SWH improves consistency between altimeters over this period.

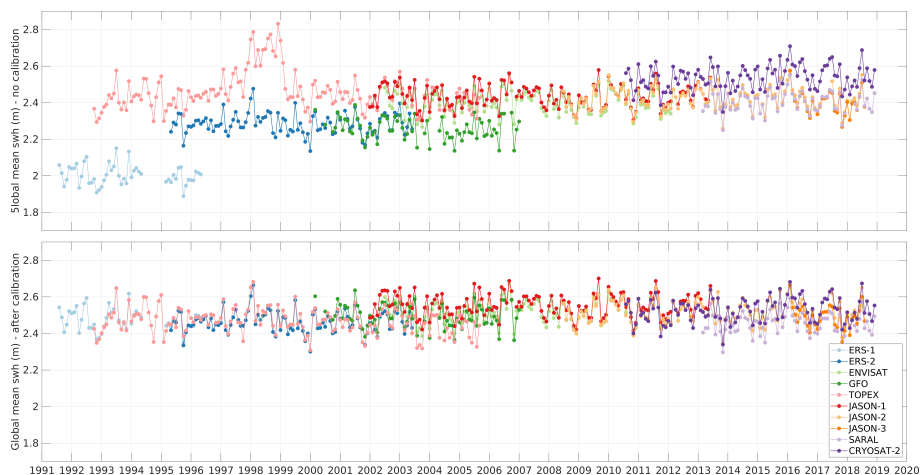


**Figure 12.** Monthly global mean SWH over the period 1991–2018 before (top panel) and after (bottom panel) calibration is applied.

## 5 Applications of the Sea State CCI dataset

### 5.1 Global wave height climatology

5 A first evaluation of the Sea State CCI dataset v1 consists in Figure 13 (top panel) of the global distribution of the climatological annual mean significant wave height calculated over the period 1992–2017. This climatological mean  $H_s$  is based on the CCI Sea State Level 4 gridded product and is presented here at the native 1 degree resolution of the CCI product. The climatology clearly shows the typical features of global wave fields, with high sea states at mid-to-high latitudes in both hemispheres corresponding to the imprint of extra-tropical storm tracks and the persistently high winds of the Southern Ocean. The 1 degree resolution of the product makes it possible also to distinguish regions of lower mean wave heights in enclosed and sheltered seas and close to islands and land, for example in the Gulf of Mexico, the Mediterranean Sea, the Baltic Sea and the Indo-Pacific Warm Pool.

15 Focusing now on the middle panel in Figure 13, we see the normalised climatological difference (expressed as a percentage of  $H_s$ ) between the CCI product and the climatological mean obtained from the calibrated multi-mission altimeter data published by Ribal and Young (2019). The overall agreement between the two altimeter-based datasets is generally good, with differences typically less than  $\pm 2.5\%$ , although some spatially coherent differences (both positive and negative) are clearly visible, most noticeably on either side of the Equator.

Finally, Figure 13 bottom panel presents a similar comparison this time between the CCI and ERA5. ERA5 (Hersbach et al., 2018) is the most recent of the reanalysis products developed and distributed by ECMWF, that features a number of



innovations, including higher spatial and temporal resolution and hourly assimilation of altimeter significant wave height data. In these results, the comparisons indicate that, even though ERA5 assimilates altimeter data, the ERA5 climatological mean  $H_s$  is substantially lower than CCI almost everywhere, except the eastern tropical Pacific and south tropical Atlantic where ERA5 clearly overestimates the wave climate. Once again, as for the comparison against Ribal & Young (2019), strong signatures are observed either side of the Equator, which are unexplained at this stage.

## 5.2 Spectral variability at regional scales

The Sea State CCI dataset v1 provides a unique opportunity to analyze global and regional sea state variability in the scale range below about 150 km. Indeed, the wave field in this scale range is strongly modulated by wave – current interactions (Ardhuin et al., 2017; Quilfen et al., 2018), hitherto neglected in the analysis of altimeter signals due to noise contamination. For illustration purpose, left panel in Figure 14 shows the three-year 2014-2016 mean surface current vorticity computed from altimeter-derived geostrophic surface currents (Rio et al., 2014) and a few regions of interest are displayed as coloured rectangles.

For these four regions, the right panel in Figure 14 shows the spectra of AltiKa 1-Hz along-track denoised measurements, with those corresponding to the global ocean for 1-Hz raw (dashed blue line) and denoised (solid blue line) SWH measurements. The differences in the spectra shown for the global ocean illustrate the noise filtering of meso-scale signals below about 150 km wavelength as explained in section 3.3. It enables a preliminary analysis of the sea state variability in the four regions highlighted. The spectra for the Drake Passage and the Agulhas Current regions are very similar in shape with higher energy levels down to 30 km. These are also regions for which the mean vorticity is very large as a consequence of the presence of very strong current gradients and eddies, and for which the wave climate is very similar. Conversely, Figure 14 also shows that spectra for the Gulf Stream and the Equator regions are very different as a consequence of different wave climates.

## 6 Current limitations and future developments

This section discusses the current status of the Sea State CCI dataset v1, the main limitations of the data and the perspectives for the future release of the dataset.

### 6.1 Definition of a reference in-situ dataset for improving altimeter calibration

Routine observations from moored buoys now exceed 40 years for several locations worldwide which make them practical for analyzing long-term trends. The most abundant open-source network is NOAA's National Data Buoy Center (NDBC) which has maintained an expansive network since the 1970's. Despite the multi-decadal time series from moored buoys, the data homogeneity is a critical issue (Gemrich et al., 2011). Buoy hulls, payloads, and data processing algorithms change over time and often the changes through meta data are not well documented. The changes in buoy configurations introduce spurious deviations in the time series at least on the same order of magnitude (if not larger) than changes due to inter-annual variability (ENSO, NAO, SAM, etc.) or secular trends. Having detailed metadata is critical to correct the buoy time series. As

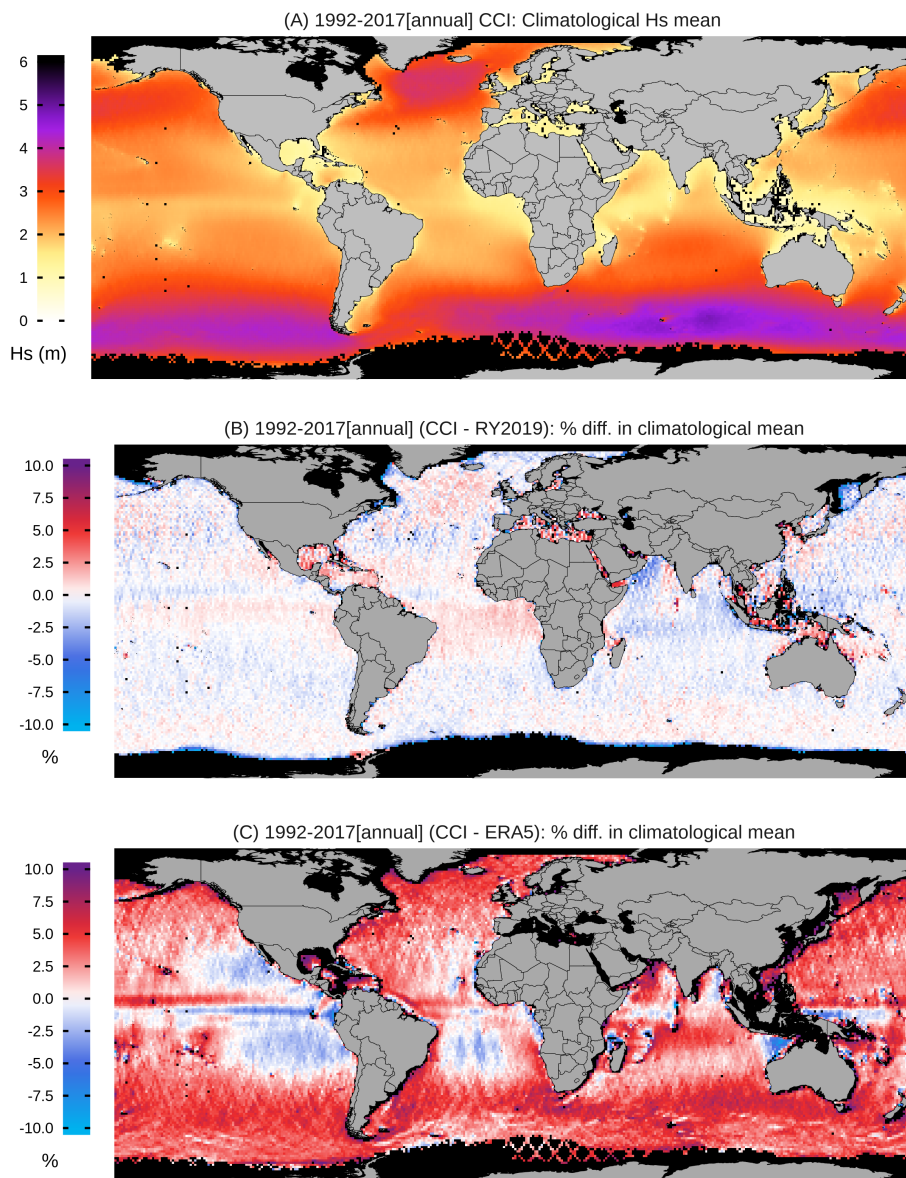


**Figure 13.** (top) Climatological annual mean SWH over the period 1992-2017 obtained with CCI v1 Level 4 data. (middle) Normalised difference (% SWH) between climatological mean from CCI and Ribal & Young, 2019. (bottom) Normalised difference (% SWH) between climatological mean from CCI and ERA5

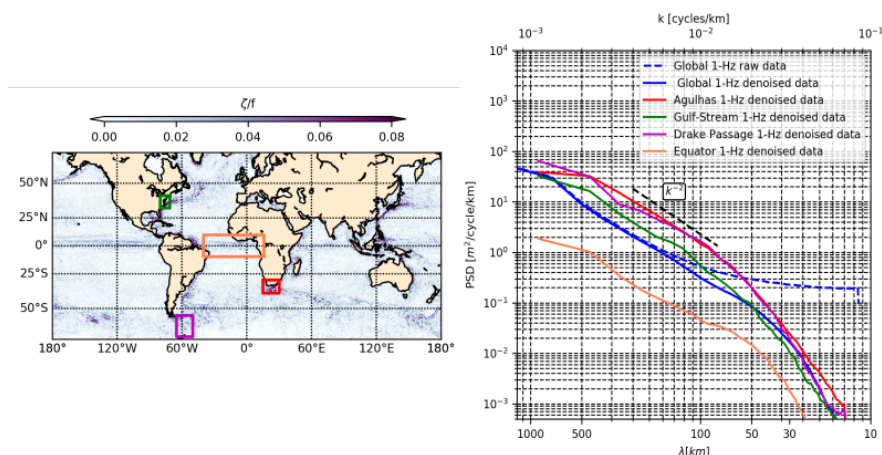


**Figure 14.** (Left panel) Global map of surface current vorticity ( $0.25^\circ \times 0.25^\circ$ ) averaged between 2014 and 2016. Colored rectangles are the studied area through a spectral analysis. (Right panel) The associated three years averaged significant wave height power spectral density (PSD) as a function of wavelength/wavenumber.

a result, reported trends from buoy records produce inconsistent results, with changes in magnitude and even sign between buoys separated by a few hundred kilometres (Allan and Komar, 2000; Gower, 2002; Ruggiero et al., 2010; Young et al., 2011). These inconsistencies mean that, at present, very few long-term buoy datasets exist which can be used reliably for trend estimation. This is a major shortcoming as no agreed “ground truth” exists to compare satellite or model estimates of trend.

- 5 There is a pressing need to produce long-term buoy datasets which include both the measured quantities of interest (significant wave height, wind speed) but also metadata documenting information such as: buoy hull type, sampling details, instrument package, processing details etc. With such metadata, it is potentially possible to correct for changes to such quantities over time and hence produce a harmonized dataset, in a similar manner to the careful reprocessing of sea surface temperature records (Merchant et al., 2019).

## 10 6.2 Assessment and implementation of new retracking algorithms

- In order to accurately estimate physical variables of relevance in satellite altimetry, average waveforms (usually at a rate of 20-Hz) are fitted to a mathematical model and an optimization algorithm, in a process called “Retracking”. For conventional (low rate mode) altimetry, all the information on SWH is encrypted in the few bins on the leading edge of the waveform (Figure 15a), which will be affected by both fading noise and, in the coastal zone, by unwanted reflections from nearby land or sheltered bays (Gomez-Enri et al., 2010); this affects the quantity of SWH estimations within 20 km of the coast (Passaro et al., 2015).
- 15 The uncertainty in estimates due to fading noise typically increases with SWH, but is much more pronounced in the near-shore region (Figure 15b). Similar challenges exist in the marginal ice zone. The advent of delay-Doppler altimetry (DDA) offers the



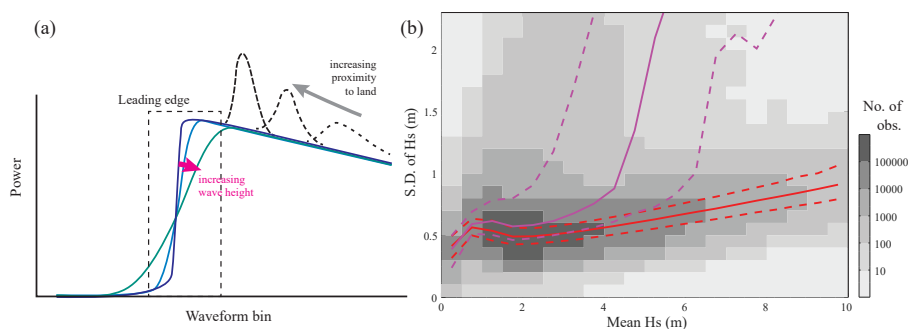


**Figure 15.** (a) Schematic of how conventional waveforms are affected by varying wave height and proximity to land. (b) Variability within a 1-second ensemble as a function of mean conditions. Illustration is from default retracker for JASON-3, with grey shading indicating the population density for open ocean conditions with the red lines indicating the 25th, 50th and 75th percentiles for 0.5 m wide bins. Pink lines show the same analysis for points within 15 km of the coast.

potential for improved SWH accuracy near land (Nencioli and Quartly, 2019) and reduced sensitivity to fading noise through "multi-looking" (Raney, 1998).

There is now a strong demand to improve the quality of altimetric wave height data through improved retracking methods in order to: 1) enhance the precision (i.e. short scale repeatability of 20 Hz estimates); 2) increase robustness and accuracy  
5 in the coastal zone and ice-affected areas; 3) observe the true spectra of waves unencumbered by retracker resolving issues such as the "spectral hump" (Dibarboure et al., 2014); 4) record accurately the extreme waves despite uncertainty increasing (Figure 15b); and 5) improve estimation at low SWH where the slope of the leading edge is inadequately resolved (Smith and Scharroo, 2015). DDA shows promise for these aspects although it is worth noting that the much narrower footprint with DDA may be leading to an underestimation bias associated with wave direction (Moreau et al., 2018).

10 To address these limitations, new retracking techniques have been developed, which generally involve one or more of the following features: numerical solution of the radar equation (as opposed to using an analytical model), fitting of a selected portion of the waveform (Passaro et al., 2014; Thibaut et al., 2017; Peng and Deng, 2018), simultaneous multi-waveform processing (Roscher et al., 2017), and post-processing aimed at reducing correlated errors among consecutive estimations (Quilfen and Chapron, 2020; Quartly et al., 2019; Quartly, 2019). On top of this, several flavours exist of an analytical model  
15 to describe the viewing geometry of the DDA acquisitions (Moreau et al., 2018; Buchhaupt et al., 2018; Ray et al., 2015).

In the framework of the Sea State CCI, a set of rules and statistics for a so-called Round Robin exercise have been defined, which is common in such projects (e.g. Brewin et al., 2015), but to date has never been applied to altimetry. The aim is to ensure that these new algorithms can be evaluated in a rigorous and transparent way, taking into account all the different applications. The procedure (Schlembach et al.) involves comparison with external datasets (buoys and models), internal analysis of outlier  
20 rejection, quality flags, precision and spectral properties. The statistics are assessed both for different distances from the coast and varying values of SWH.





## 7 Conclusions

The Climate Change Initiative program launched by ESA in 2010 has fostered the production of climate-quality long-term global datasets of Essential Climate Variables, whose analysis is needed for understanding the mechanisms of climate change and associated societal impact. In this context, the Sea State CCI project is in charge of reprocessing and developing dedicated algorithms for historical and current EO missions dedicated to the observations of sea state (radar altimeters and SAR missions) in order to produce a continuous, consistent and robust long-term dataset of sea state parameters. The first version of the Sea State CCI dataset, presented in this study, covers the period 1991-2018 and includes observations from 10 altimeter missions. The implementation of quality flags and auxiliary parameters in a systematic way, the update of calibration formula for the most recent missions, the development of an EMD-based denoising method and the validation against an extensive network of in-situ data buoys as well as state-of-the art model results, resulted in a unique dataset designed for the study of wave climate variability. This dataset has already proved really useful to investigate sea state variability at global and regional scales, in terms of wave climatology and spectral variability. Future releases of the Sea State CCI dataset will extend even further the capacity of this dataset, through 1) the implementation of dedicated retracking algorithms for estimating the SWH with improved accuracy; 2) the revision of calibration formula based on a high-quality and consistent data set of in-situ buoys measurements; and 3) the inclusion of spectral wave parameters derived from SAR missions.

## 8 Data availability

The Sea State CCI dataset v1 is freely available on the ESA CCI website (<http://cci.esa.int/data>) at [ftp://anon-ftp.ceda.ac.uk/neodc/esacci/sea\\_state/data/v1.1\\_release/](ftp://anon-ftp.ceda.ac.uk/neodc/esacci/sea_state/data/v1.1_release/). Three products are available: a multi-mission along-track L2P product (<http://dx.doi.org/10.5285/f91cd3ee7b6243d5b7d41b9beaf397e1>, Piollé et al., 2020a), a daily merged multi mission along-track L3 product (<http://dx.doi.org/10.5285/3ef6a5a66e9947d39b356251909dc12b>, Piollé et al., 2020b) and a multi-mission monthly gridded L4 product (<http://dx.doi.org/10.5285/47140d618dcc40309e1edbc7e773478>, Piollé et al., 2020c).

*Competing interests.* The authors declare that they have no competing interests.

*Acknowledgements.* All authors are supported by the European Space Agency under the Sea State Climate Change Initiative project.



## References

- Allan, J. and Komar, P.: Are ocean wave heights increasing in the eastern North Pacific?, *Eos, Transactions American Geophysical Union*, 81, 561–567, <https://doi.org/10.1029/EO081i047p00561-01>, <https://agupubs.onlinelibrary.wiley.com/doi/abs/10.1029/EO081i047p00561-01>, 2000.
- 5 Arduin, F., Gille, S. T., Menemenlis, D., Rocha, C. B., Raschle, N., Chapron, B., Gula, J., and Molemaker, J.: Small-scale open ocean currents have large effects on wind wave heights, *Journal of Geophysical Research: Oceans*, 122, 4500–4517, <https://doi.org/10.1002/2016JC012413>, <https://agupubs.onlinelibrary.wiley.com/doi/abs/10.1002/2016JC012413>, 2017.
- Arduin, F., Stopa, J. E., Chapron, B., Collard, F., Husson, R., Jensen, R. E., Johannessen, J., Mouche, A., Passaro, M., Quartly, G. D., Swail, V., and Young, I.: Observing Sea States, *Frontiers in Marine Science*, 6, <https://doi.org/10.3389/fmars.2019.00124>, <https://www.frontiersin.org/articles/10.3389/fmars.2019.00124/full>, 2019.
- 10 Babanin, A. V. and Haus, B. K.: On the Existence of Water Turbulence Induced by Nonbreaking Surface Waves, *Journal of Physical Oceanography*, 39, 2675–2679, <https://doi.org/10.1175/2009JPO4202.1>, <https://journals.ametsoc.org/doi/full/10.1175/2009JPO4202.1>, 2009.
- Brewin, R. J., Sathyendranath, S., Müller, D., Brockmann, C., Deschamps, P.-Y., Devred, E., Doerffer, R., Fomferra, N., Franz, B., Grant, M., Groom, S., Horseman, A., Hu, C., Krasemann, H., Lee, Z., Maritorena, S., Mélin, F., Peters, M., Platt, T., Regner, P., Smyth, T., Steinmetz, F., Swinton, J., Werdell, J., and White, G. N.: The Ocean Colour Climate Change Initiative: III. A round-robin comparison on in-water bio-optical algorithms, *Remote Sensing of Environment*, 162, 271 – 294, <https://doi.org/https://doi.org/10.1016/j.rse.2013.09.016>, <http://www.sciencedirect.com/science/article/pii/S0034425713003519>, 2015.
- 15 Buchhaupt, C., Fenoglio-Marc, L., Dinardo, S., Scharroo, R., and Becker, M.: A fast convolution based waveform model for conventional and unfocused SAR altimetry, *Advances in Space Research*, 62, 1445 – 1463, <https://doi.org/https://doi.org/10.1016/j.asr.2017.11.039>, <http://www.sciencedirect.com/science/article/pii/S0273117717308505>, the CryoSat Satellite Altimetry Mission: Eight Years of Scientific Exploitation, 2018.
- Dibarboure, G., Boy, F., Desjonqueres, J. D., Labroue, S., Lasne, Y., Picot, N., Poisson, J. C., and Thibaut, P.: Investigating Short-Wavelength Correlated Errors on Low-Resolution Mode Altimetry, *Journal of Atmospheric and Oceanic Technology*, 31, 1337–1362, <https://doi.org/10.1175/JTECH-D-13-00081.1>, <https://doi.org/10.1175/JTECH-D-13-00081.1>, 2014.
- 25 Edson, J. B., Jampana, V., Weller, R. A., Bigorre, S. P., Plueddemann, A. J., Fairall, C. W., Miller, S. D., Mahrt, L., Vickers, D., and Hersbach, H.: On the Exchange of Momentum over the Open Ocean, *Journal of Physical Oceanography*, 43, 1589–1610, <https://doi.org/10.1175/JPO-D-12-0173.1>, <https://journals.ametsoc.org/doi/full/10.1175/JPO-D-12-0173.1>, 2013.
- Flandrin, P., Rilling, G., and Goncalves, P.: Empirical mode decomposition as a filter bank, *IEEE Signal Processing Letters*, 11, 112–114, <https://doi.org/10.1109/LSP.2003.821662>, 2004.
- 30 Gemmrich, J., Thomas, B., and Bouchard, R.: Observational changes and trends in northeast Pacific wave records, *Geophysical Research Letters*, 38, <https://doi.org/10.1029/2011GL049518>, <https://agupubs.onlinelibrary.wiley.com/doi/abs/10.1029/2011GL049518>, 2011.
- GlobWaveTeam: Deliverable D.18. Annual Quality Control Report - Phase 2, Tech. rep., [http://globwave.ifremer.fr/download/GlobWave\\_D\\_18\\_AQCR.pdf](http://globwave.ifremer.fr/download/GlobWave_D_18_AQCR.pdf), 2012.
- GlobWaveTeam: Deliverable D.30. GlobWave Final Report, Tech. rep., <http://globwave.ifremer.fr/news/wave-community/item/511-globwave-final-report-now-available>, 2013.
- 35



- Gomez-Enri, J., Vignudelli, S., Quartly, G. D., Gommenginger, C. P., Cipollini, P., Challenor, P. G., and Benveniste, J.: Modeling Envisat RA-2 Waveforms in the Coastal Zone: Case Study of Calm Water Contamination, *IEEE Geoscience and Remote Sensing Letters*, 7, 474–478, <https://doi.org/10.1109/LGRS.2009.2039193>, 2010.
- Gower, J. F. R.: Temperature, Wind and Wave Climatologies, and Trends from Marine Meteorological Buoys in the Northeast Pacific, *Journal of Climate*, 15, 3709–3718, [https://doi.org/10.1175/1520-0442\(2002\)015<3709:TWAWCA>2.0.CO;2](https://doi.org/10.1175/1520-0442(2002)015<3709:TWAWCA>2.0.CO;2), <https://journals.ametsoc.org/doi/full/10.1175/1520-0442%282002%29015%3C3709%3ATWAWCA%3E2.0.CO%3B2>, 2002.
- Gulev, S. K. and Grigorieva, V.: Last century changes in ocean wind wave height from global visual wave data, *Geophysical Research Letters*, 31, <https://doi.org/10.1029/2004GL021040>, <https://agupubs.onlinelibrary.wiley.com/doi/abs/10.1029/2004GL021040>, 2004.
- Hersbach, H., de Rosnay, P., Bell, B., Schepers, D., Simmons, A., Soci, C., Abdalla, S., Alonso-Balmaseda, M., Balsamo, G., Bechtold, P., Berrisford, P., Bidlot, J.-R., de Boissésón, E., Bonavita, M., Browne, P., Buizza, R., Dahlgren, P., Dee, D., Dragani, R., Diamantakis, M., Flemming, J., Forbes, R., Geer, A., Haiden, T., Hólm, E., Haimberger, L., Hogan, R., Horányi, A., Janiskova, M., Laloyaux, P., Lopez, P., Muñoz-Sabater, J., Peubey, C., Radu, R., Richardson, D., Thépaut, J.-N., Vitart, F., Yang, X., Zsótér, E., and Zuo, H.: Operational global reanalysis: progress, future directions and synergies with NWP, Tech. rep., European Centre for Medium Range Weatherforecasting, <https://doi.org/10.21957/tkic6g3wm>, <https://www.ecmwf.int/en/elibrary/18765-operational-global-reanalysis-progress-future-directions-and-synergies-nwp>, 2018.
- Huang, N. E., Shen, Z., Long, S. R., Wu, M. C., Shih, H. H., Zheng, Q., Yen, N.-C., Tung, C. C., and Liu, H. H.: The empirical mode decomposition and the Hilbert spectrum for nonlinear and non-stationary time series analysis, *Proceedings of the Royal Society of London A: Mathematical, Physical and Engineering Sciences*, 454, 903–995, <https://doi.org/10.1098/rspa.1998.0193>, <http://rspa.royalsocietypublishing.org/content/454/1971/903>, 1998.
- Kopsinis, Y. and McLaughlin, S.: Development of EMD-Based Denoising Methods Inspired by Wavelet Thresholding, *IEEE Transactions on Signal Processing*, 57, 1351–1362, <https://doi.org/10.1109/TSP.2009.2013885>, 2009.
- Kraus, N. C. and Wamsley, T. V.: Coastal Barrier Breaching. Part 1. Overview of Breaching Processes, Tech. rep., ENGINEER RESEARCH AND DEVELOPMENT CENTER VICKSBURG MS COASTAL AND HYDRAULICS LAB, <https://apps.dtic.mil/docs/citations/ADA588872>, 2003.
- Lavergne, T., Sørensen, A. M., Kern, S., Tonboe, R., Notz, D., Aaboe, S., Bell, L., Dybkjær, G., Eastwood, S., Gabarro, C., Heygster, G., Killie, M. A., Brandt Kreiner, M., Lavelle, J., Saldo, R., Sandven, S., and Pedersen, L. T.: Version 2 of the EUMETSAT OSI SAF and ESA CCI sea-ice concentration climate data records, *The Cryosphere*, 13, 49–78, <https://doi.org/https://doi.org/10.5194/tc-13-49-2019>, <https://www.the-cryosphere.net/13/49/2019/>, 2019.
- Longuet-Higgins, M. S. and Stewart, R. W.: Radiation stress and mass transport in gravity waves, with application to ‘surf beats’, *Journal of Fluid Mechanics*, 13, 481, <https://doi.org/10.1017/S0022112062000877>, [http://www.journals.cambridge.org/abstract\\_S0022112062000877](http://www.journals.cambridge.org/abstract_S0022112062000877), 1962.
- Masselink, G., Castelle, B., Scott, T., Dodet, G., Suanez, S., Jackson, D., and Floc’h, F.: Extreme wave activity during 2013/2014 winter and morphological impacts along the Atlantic coast of Europe, *Geophysical Research Letters*, p. 2015GL067492, <https://doi.org/10.1002/2015GL067492>, <http://onlinelibrary.wiley.com/doi/10.1002/2015GL067492/abstract>, 2016.
- Merchant, C. J., Embury, O., Bulgin, C. E., Block, T., Corlett, G. K., Fiedler, E., Good, S. A., Mittaz, J., Rayner, N. A., Berry, D., Eastwood, S., Taylor, M., Tsushima, Y., Waterfall, A., Wilson, R., and Donlon, C.: Satellite-based time-series of sea-surface temperature since 1981 for climate applications, *Scientific Data*, 6, 1–18, <https://doi.org/10.1038/s41597-019-0236-x>, <https://www.nature.com/articles/s41597-019-0236-x>, 2019.



- Monahan, E. C., Spiel, D. E., and Davidson, K. L.: A Model of Marine Aerosol Generation Via Whitecaps and Wave Disruption, in: Oceanic Whitecaps: And Their Role in Air-Sea Exchange Processes, edited by Monahan, E. C. and Niocaill, G. M., Oceanographic Sciences Library, pp. 167–174, Springer Netherlands, Dordrecht, [https://doi.org/10.1007/978-94-009-4668-2\\_16](https://doi.org/10.1007/978-94-009-4668-2_16), [https://doi.org/10.1007/978-94-009-4668-2\\_16](https://doi.org/10.1007/978-94-009-4668-2_16), 1986.
- 5 Moreau, T., Tran, N., Aublanc, J., Tison, C., Gac, S. L., and Boy, F.: Impact of long ocean waves on wave height retrieval from SAR altimetry data, *Advances in Space Research*, 62, 1434 – 1444, <https://doi.org/https://doi.org/10.1016/j.asr.2018.06.004>, <http://www.sciencedirect.com/science/article/pii/S0273117718304708>, the CryoSat Satellite Altimetry Mission: Eight Years of Scientific Exploitation, 2018.
- Nencioli, F. and Quartly, G. D.: Evaluation of Sentinel-3A Wave Height Observations Near the Coast of Southwest England, *Remote Sensing*, 11, <https://doi.org/10.3390/rs11242998>, <https://www.mdpi.com/2072-4292/11/24/2998>, 2019.
- 10 Passaro, M., Cipollini, P., Vignudelli, S., Quartly, G. D., and Snaith, H. M.: ALES: A multi-mission adaptive sub-waveform retracker for coastal and open ocean altimetry, *Remote Sensing of Environment*, 145, 173 – 189, <https://doi.org/https://doi.org/10.1016/j.rse.2014.02.008>, <http://www.sciencedirect.com/science/article/pii/S0034425714000534>, 2014.
- Passaro, M., Fenoglio-Marc, L., and Cipollini, P.: Validation of Significant Wave Height From Improved Satellite Altimetry in the German Bight, *IEEE Transactions on Geoscience and Remote Sensing*, 53, 2146–2156, <https://doi.org/10.1109/TGRS.2014.2356331>, 2015.
- 15 Peng, F. and Deng, X.: A New Retracking Technique for Brown Peaky Altimetric Waveforms, *Marine Geodesy*, 41, 99–125, <https://doi.org/10.1080/01490419.2017.1381656>, <https://doi.org/10.1080/01490419.2017.1381656>, 2018.
- Piollé, J.-F., Dodet, G., and Quilfen, Y.: ESA Sea State Climate Change Initiative (Sea\_State\_cci): Global remote sensing multi-mission along-track significant wave height, L2P product, version 1.1, Centre for Environmental Data Analysis, <https://doi.org/http://dx.doi.org/10.5285/f91cd3ee7b6243d5b7d41b9beaf397e1>, 2020a.
- 20 Piollé, J.-F., Dodet, G., and Quilfen, Y.: ESA Sea State Climate Change Initiative (Sea\_State\_cci) : Global remote sensing daily merged multi-mission along-track significant wave height, L3 product, version 1.1., Centre for Environmental Data Analysis, <https://doi.org/http://dx.doi.org/10.5285/3ef6a5a66e9947d39b356251909dc12b>, 2020b.
- Piollé, J.-F., Dodet, G., and Quilfen, Y.: ESA Sea State Climate Change Initiative (Sea\_State\_cci) : Global remote sensing merged multi-mission monthly gridded significant wave height, L4 product, version 1.1., Centre for Environmental Data Analysis, <https://doi.org/http://dx.doi.org/10.5285/47140d618dcc40309e1edbca7e773478>, 2020c.
- 25 Popp, T., De Leeuw, G., Bingen, C., Brühl, C., Capelle, V., Chedin, A., Clarisse, L., Dubovik, O., Grainger, R., Griesfeller, J., Heckel, A., Kinne, S., Klüser, L., Kosmale, M., Kolmonen, P., Lelli, L., Litvinov, P., Mei, L., North, P., Pinnock, S., Povey, A., Robert, C., Schulz, M., Sogacheva, L., Stebel, K., Stein Zweers, D., Thomas, G., Tilstra, L. G., Vandenbussche, S., Veeffkind, P., Vountas, M., and Xue, Y.: Development, Production and Evaluation of Aerosol Climate Data Records from European Satellite Observations (Aerosol\_cci), *Remote Sensing*, 8, 421, <https://doi.org/10.3390/rs8050421>, <https://www.mdpi.com/2072-4292/8/5/421>, 2016.
- 30 Quartly, G. D.: Removal of Covariant Errors from Altimetric Wave Height Data, *Remote Sensing*, 11, <https://doi.org/10.3390/rs11192319>, <https://www.mdpi.com/2072-4292/11/19/2319>, 2019.
- Quartly, G. D., Legeais, J.-F., Ablain, M., Zawadzki, L., Fernandes, M. J., Rudenko, S., Carrère, L., García, P. N., Cipollini, P., Andersen, O. B., Poisson, J.-C., Mbajon Njiche, S., Cazenave, A., and Benveniste, J.: A new phase in the production of quality-controlled sea level data, *Earth System Science Data*, 9, 557–572, <https://doi.org/10.5194/essd-9-557-2017>, <https://www.earth-syst-sci-data.net/9/557/2017/>, 2017.
- Quartly, G. D., Smith, W. H. F., and Passaro, M.: Removing Intra-1-Hz Covariant Error to Improve Altimetric Profiles of  $\sigma^0$  and Sea Surface Height, *IEEE Transactions on Geoscience and Remote Sensing*, 57, 3741–3752, <https://doi.org/10.1109/TGRS.2018.2886998>, 2019.



- Queffelec, P.: Long-Term Validation of Wave Height Measurements from Altimeters, *Marine Geodesy*, 27, 495–510, <https://doi.org/10.1080/01490410490883478>, <https://doi.org/10.1080/01490410490883478>, 2004.
- Queffelec, P. and Croizé-Fillon, D.: Global altimeter SWH data set, Tech. rep., IFREMER, [ftp://ftp.ifremer.fr/ifremer/cersat/products/swath/altimeters/waves/documentation/altimeter\\_wave\\_merge\\_\\_11.4.pdf](ftp://ftp.ifremer.fr/ifremer/cersat/products/swath/altimeters/waves/documentation/altimeter_wave_merge__11.4.pdf), 2017.
- 5 Quilfen, Y. and Chapron, B.: Ocean Surface Wave-Current Signatures From Satellite Altimeter Measurements, *Geophysical Research Letters*, 46, 253–261, <https://doi.org/10.1029/2018GL081029>, <https://agupubs.onlinelibrary.wiley.com/doi/abs/10.1029/2018GL081029>, 2019.
- Quilfen, Y. and Chapron, B.: On denoising satellite altimeter measurements for high-resolution geophysical signal analysis, Submitted to *Advances in Space Research*, 2020.
- Quilfen, Y., Yurovskaya, M., Chapron, B., and Ardhuin, F.: Storm waves focusing and steepening in the Agulhas current: Satellite observations and modeling, *Remote Sensing Of Environment*, 216, 561–571, <https://doi.org/10.1016/j.rse.2018.07.020>, <https://archimer.ifremer.fr/doc/00451/56289/>, 2018.
- 10 Raney, R. K.: The delay/Doppler radar altimeter, *IEEE Transactions on Geoscience and Remote Sensing*, 36, 1578–1588, <https://doi.org/10.1109/36.718861>, 1998.
- Rascle, N. and Ardhuin, F.: A global wave parameter database for geophysical applications. Part 2: model validation with improved source term parameterization, *Oceanogr. Meteorol.*, 70, 174–188, <https://doi.org/10.1016/j.ocemod.2012.12.001>, 2013.
- 15 Ray, C., Martin-Puig, C., Clarizia, M. P., Ruffini, G., Dinardo, S., Gommenginger, C., and Benveniste, J.: SAR Altimeter Backscattered Waveform Model, *IEEE Transactions on Geoscience and Remote Sensing*, 53, 911–919, <https://doi.org/10.1109/TGRS.2014.2330423>, 2015.
- Ribal, A. and Young, I. R.: 33 years of globally calibrated wave height and wind speed data based on altimeter observations, *Scientific Data*, 20 6, 77, <https://doi.org/10.1038/s41597-019-0083-9>, <https://www.nature.com/articles/s41597-019-0083-9>, 2019.
- Rio, M.-H., Mulet, S., and Picot, N.: Beyond GOCE for the ocean circulation estimate: Synergetic use of altimetry, gravimetry, and in situ data provides new insight into geostrophic and Ekman currents, *Geophysical Research Letter*, 41, <https://doi.org/doi:10.1002/2014GL061773>, 2014.
- Roscher, R., Uebbing, B., and Kusche, J.: STAR: Spatio-temporal altimeter waveform retracking using sparse representation and conditional random fields, *Remote Sensing of Environment*, 201, 148 – 164, <https://doi.org/https://doi.org/10.1016/j.rse.2017.07.024>, <http://www.sciencedirect.com/science/article/pii/S0034425717303395>, 2017.
- 25 Ruggiero, P., Komar, P. D., and Allan, J. C.: Increasing wave heights and extreme value projections: The wave climate of the U.S. Pacific Northwest, *Coastal Engineering*, 57, 539–552, <https://doi.org/10.1016/j.coastaleng.2009.12.005>, <http://www.sciencedirect.com/science/article/pii/S0378383909002142>, 2010.
- 30 Schlembach, F., Passaro, M., Quartly, G. D., Kurekin, A., and others, *journal=Remote Sensing*, t. y.: .
- Sepulveda, H., Queffelec, P., and Ardhuin, F.: Assessment of SARAL/AltiKa Wave Height Measurements Relative to Buoy, Jason-2, and Cryosat-2 Data, *Marine Geodesy*, 38, 449–465, <https://doi.org/10.1080/01490419.2014.1000470>, <https://archimer.ifremer.fr/doc/00286/39675/>, 2015.
- Smith, W. H. F. and Scharroo, R.: Waveform Aliasing in Satellite Radar Altimetry, *IEEE Transactions on Geoscience and Remote Sensing*, 35 53, 1671–1682, <https://doi.org/10.1109/TGRS.2014.2331193>, 2015.
- Stopa, J. E., Sutherland, P., and Ardhuin, F.: Strong and highly variable push of ocean waves on Southern Ocean sea ice, *Proceedings of the National Academy of Sciences*, 115, 5861–5865, <https://doi.org/10.1073/pnas.1802011115>, <http://www.pnas.org/content/115/23/5861>, 2018.



- The WAVEWATCH III Development Group: User manual and system documentation of WAVEWATCH III version 5.16, NOAA/NWS/NCEP/MMAB Technical Note 316, p. 326, [http://polart.ncep.noaa.gov/mmab/papers/tn276/MMAB\\_276.pdf](http://polart.ncep.noaa.gov/mmab/papers/tn276/MMAB_276.pdf), 2016.
- Thibaut, P., Poisson, J., Bronner, E., and Picot, N.: Relative performance of the MLE3 and MLE4 retracking algorithms on Jason-2 altimeter waveforms, *Mar. Geod.*, 33, 317–335, 2010.
- 5 Thibaut, P., Piras, F., Poisson, J. C., Moreau, T., Halimi, A., Boy, F., and Guillot, A.: Convergent solutions for retracking conventional and Delay Doppler altimeter echoes, in: *Proceedings of the Ocean Surface Topography Science Team Meeting*, p. 18, Miami, [https://meetings.aviso.altimetry.fr/fileadmin/user\\_upload/IPM\\_06\\_Thibaut\\_LRM\\_SAR\\_Retrackers\\_-\\_16.9.pdf](https://meetings.aviso.altimetry.fr/fileadmin/user_upload/IPM_06_Thibaut_LRM_SAR_Retrackers_-_16.9.pdf), 2017.
- Thornton, E. B., Humiston, R. T., and Birkemeier, W.: Bar/trough generation on a natural beach, *Journal of Geophysical Research: Oceans*, 101, 12 097–12 110, <https://doi.org/10.1029/96JC00209>, <https://agupubs.onlinelibrary.wiley.com/doi/abs/10.1029/96JC00209>, 1996.
- 10 Tournadre, J., Bouhier, N., Girard-Ardhuin, F., and Rémy, F.: Antarctic icebergs distributions 1992–2014, *Journal of Geophysical Research: Oceans*, 121, 327–349, <https://doi.org/10.1002/2015JC011178>, <https://agupubs.onlinelibrary.wiley.com/doi/abs/10.1002/2015JC011178>, 2016.
- Tran, N., Vandemark, D., Zaron, E. D., Thibaut, P., Dibarboure, G., and Picot, N.: Assessing the effects of sea-state related errors on the precision of high-rate Jason-3 altimeter sea level data, *Advances in Space Research*, <https://doi.org/10.1016/j.asr.2019.11.034>, <http://www.sciencedirect.com/science/article/pii/S0273117719308427>, 2019.
- 15 Wentz, F., Hilburn, K., and Smith, D.: Remote Sensing Systems DMSP SSM/I Daily Environmental Suite on 0.25 deg grid, Version 7. Remote Sensing Systems, Santa Rosa, CA., Remote Sensing Systems, <http://www.remss.com/missions/ssmi/>, 2012.
- Young, I. R. and Ribal, A.: Multiplatform evaluation of global trends in wind speed and wave height, *Science*, 364, 548, <https://doi.org/10.1126/science.aav9527>, <http://science.sciencemag.org/content/364/6440/548.abstract>, 2019.
- 20 Young, I. R., Zieger, S., and Babanin, A. V.: Global Trends in Wind Speed and Wave Height, *Science*, 332, 451–455, <https://doi.org/10.1126/science.1197219>, <http://www.sciencemag.org/cgi/doi/10.1126/science.1197219>, 2011.
- Zieger, S., Vinoth, J., and Young, I. R.: Joint Calibration of Multiplatform Altimeter Measurements of Wind Speed and Wave Height over the Past 20 Years, *Journal of Atmospheric and Oceanic Technology*, 26, 2549–2564, <https://doi.org/10.1175/2009JTECHA1303.1>, <https://journals.ametsoc.org/doi/10.1175/2009JTECHA1303.1>, 2009.